

Fluid Echoes in a Pure Electron Plasma

J. H. Yu, T. M. O'Neil, and C. F. Driscoll

*Physics Department and Institute for Pure and Applied Physical Sciences, University of California at San Diego,
La Jolla, California 92093, USA*

(Received 17 August 2004; published 19 January 2005)

Experimental observations of diocotron wave echoes on a magnetized electron column are reported, representing Kelvin wave echoes on a rotating near-ideal fluid. The echoes occur by reversal of an inviscid wave damping process, and the phase-space mixing and unmixing are directly imaged. The basic echo characteristics agree with a simple nonlinear ballistic theory. At late times, the echo is degraded, and the maximal observed echo times agree with a theory of electron-electron collisions acting on separately evolving velocity classes.

DOI: 10.1103/PhysRevLett.94.025005

PACS numbers: 52.27.Jt, 47.15.Ki, 47.32.Cc

Echoes appear in relaxation processes in a variety of systems, including the spin echo [1], cyclotron echo [2], photon echo [3], and plasma wave echo [4,5]. In general, echo phenomena involve a macroscopic signal that damps away because of nondissipative phase mixing. This phase mixing is then (partially) reversed by application of a second wave, and a macroscopic signal reappears later in time as the echo. The echo provides an explicit demonstration that the damping is thermodynamically reversible.

Since the echo depends on the maintenance of phase coherence during the mixing and unmixing process, it is an exquisitely sensitive probe of effects that destroy coherence. For example, the beam echo was used to measure a 10^{-4} s^{-1} intrabeam collision frequency for a coasting antiproton beam at Fermilab [6], and a 10^{-13} s^{-1} collision frequency for a higher energy coasting proton beam at CERN [7].

This Letter reports the first experimental observation of surface wave echoes on a near-ideal 2D vortex, using a magnetized electron column as the “working fluid.” The z -averaged $\mathbf{E} \times \mathbf{B}$ drift dynamics of the electron column is isomorphic to the (r, θ) dynamics of an ideal (incompressible and inviscid) fluid [8], so the echoes represent Kelvin wave [9] echoes. Following theory and simulation work of Gould and Bachman [10], we adopt the name *fluid echo*. We demonstrate that the echo mode number and appearance time agree with a simple nonlinear ballistic theory and find that the maximal echo lifetime is fundamentally limited by electron-electron collisions, but can also be limited by large amplitude effects.

To produce the fluid echo, we first launch a surface drift wave on a quiescent electron column with density $n_0(r)$. These surface waves (diocotron waves) [11] have density perturbation $\delta n_i(r)e^{i(m_i\theta - \omega_i t)}$ and are essentially uniform in z . The measured wave electric field at the cylindrical wall is proportional to the radial integral over δn . For our chosen profiles $n(r)$, the excited wave rapidly damps away by the phase mixing of spatial Landau damping [12]: strong radial shear in the $\mathbf{E} \times \mathbf{B}$ rotation frequency $\omega_E(r)$ causes progressive spiral windup of the perturbation

$\delta n_i(r, \theta, t)$, so the wave potential $\delta\phi$ phase mixes to zero. Although the wave potential vanishes, an intricate phase-mixing pattern remains stored in $\delta n_i(r, \theta, t)$.

After some time τ , a second diocotron wave is launched and it too damps away, leaving its own phase-mixing pattern $\delta n_s(r, \theta, t)$. The second wave excitation also modulates the perturbation remaining from the first wave, producing a second-order perturbation $\delta n^{(2)}(r, \theta, t)$. This second-order perturbation begins to unmix, and it eventually produces a wave electric field which is the echo.

This simple description of the 2D echo is complicated by 3D “end” effects which make ω_E dependent on an electron's z -velocity, i.e. $\omega_E(r, v_z)$ [13]. That is, energetic electrons penetrate further into the end confinement potential, and therefore have a different z -averaged $\omega_E(r, v_z)$. Different z -velocity classes must *separately* phase mix and unmix to form a combined echo, and collisional velocity scatterings fundamentally limit this recombination.

The fluid echoes are close cousins of plasma wave echoes [4,5]. Indeed, the description of a plasma wave echo differs from the above 2D description only in that the wave electric field is given by an integral over the perturbation in the phase-space distribution $\delta f(z, p_z, t)$.

For (z, p_z) plasma wave echoes, the phase-space distribution $f(z, p_z)$ evolves according to the Vlasov equation

$$\frac{\partial f}{\partial t} + [f, H_z] = 0, \quad (1)$$

where $[f, H_z]$ is a Poisson bracket and $H_z = p_z^2/2M - e\delta\phi(z, t)$ is the Hamiltonian for 1D electron dynamics.

For fluid echoes, the continuity equation can be written as a “Vlasov” equation

$$\frac{\partial n}{\partial t} + [n, H] = 0, \quad (2)$$

where $H = e\phi_0(r) + e\delta\phi(r, \theta, t)$ is the guiding center drift Hamiltonian. The perturbed potential $\delta\phi$ includes any externally applied vacuum potentials and could include the collective plasma response, but all self-consistent wave effects are neglected here. Of course, when calculat-

ing the echo response, the potential perturbation from the perturbed density must be calculated.

The phase space (θ, p_θ) corresponds directly to configuration space (θ, r^2) , because the angular momentum in $\mathbf{E} \times \mathbf{B}$ drift dynamics is given by $p_\theta = (eB/2c)r^2$ [12]. Thus, the phase mixing and unmixing are observed directly in measurements of $n(r, \theta, t)$.

The cylindrical Penning-Malmberg trap and imaging diagnostic are shown in Fig. 1. Electrons are trapped in vacuum (10^{-10} torr) inside a series of conducting cylinders ($R_w = 3.5$ cm). End voltages ($V_c = -100$ V) confine the electrons axially, and the axial magnetic field ($\mathbf{B} = 1\text{--}4$ kG $\hat{\mathbf{z}}$) provides radial confinement.

The trapped electron column typically has a density $n_0 \approx 10^7$ cm $^{-3}$, radius $R_p \approx 1.6$ cm with a broad tail, and length $L \approx 50$ cm. The electrons have average kinetic energy $T \approx 5$ eV, giving a rapid axial bounce frequency $f_b \approx \bar{v}/2L \approx 1$ MHz (where $\bar{v} \equiv \sqrt{T/M}$), and giving a negligibly small cyclotron radius $r_c \lesssim 15$ μ m. The electron space charge creates a radial electric field $E(r) = -\partial\phi_0/\partial r$, resulting in a bounce-averaged $\mathbf{E} \times \mathbf{B}$ drift rotation rate $\omega_E(r, v_z) \equiv \langle cE(r, z)/Br \rangle_b \approx 2\pi \times 50$ kHz. The v_z dependence of ω_E is ignored until collisional effects are treated.

At a chosen time in the evolution, the z -integrated electron density $n(r, \theta, t)$ is measured by dumping the plasma onto a phosphor screen (biased to 15 kV), imaged by a low-noise 512×512 CCD camera. The shot-to-shot reproducibility is good [$\delta n(r)/n \approx 0.1\%$], so a time evolution is obtained by creating a sequence of plasmas with identical wave excitations, each dumped at differing times t .

At $t = 0$ an initial wave, with $m_i = 2$ and $\omega_i = 2\pi \times 20$ kHz, is excited by applying a voltage $V_i = 0.2\text{--}10$ V to two 180° -opposed wall sectors for a time $\Delta t_i \sim \pi/\omega_i$. Figure 2(a)–2(c) shows the received wall signal as the wave damps away. The corresponding 2D density is initially “circular,” i.e., $n_0(r)$, but it is distorted into an elliptical $n(r, \theta)$ by the initial excitation.

The “perturbation” images of Fig. 2 have the symmetric equilibrium subtracted out, displaying $\delta n(r, \theta, t) \equiv$

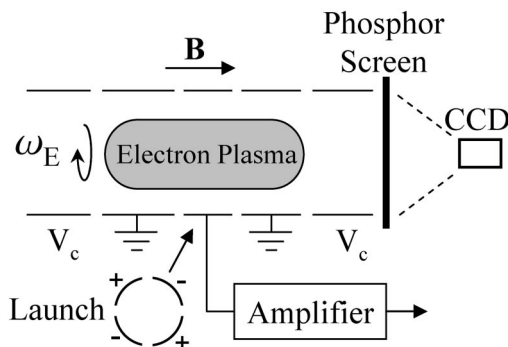


FIG. 1. Electron trap with CCD camera density diagnostic. The wall signal from sector electrodes is used to measure the wave amplitudes.

$n(r, \theta, t) - n_0(r)$. The colors show magnitude of δn ; the initial amplitude is $|\delta n| \approx 10^{-2}n(r)$, but the color scale is adjusted from image to image to maximize the visibility. The elliptical distortion rotates at frequency ω_i , but in ~ 5 wave periods it damps back to a circular cross section due to spatial Landau damping, with spiral windup of the density perturbation.

At time τ , a second wave with $m_s = 4$ is excited by applying a voltage $V_s = 0.2\text{--}10$ V to four sectors for $\Delta t_s \sim \pi/\omega_s$. (The visible wall signal represents a spurious coupling of the $m_s = 4$ excitation into the $m = 2$ detection electronics.) The remnants of the phase-mixed initial wave are visible as thin filaments in Fig. 2(d). The second wave excitation causes θ -dependent radial shifts of the filaments, so the filaments $\mathbf{E} \times \mathbf{B}$ rotate at a new rate.

The third wave packet visible in Fig. 2 is the received $m_e = 2$ echo. The initial wave damping effectively unmixed producing an $m_e = 2$ echo response. The peak echo wall signal S_e occurs at a time $t \approx 2\tau$ for the mode numbers used here. The corresponding image 2(h) shows $|\delta n| \approx 0.3 \times 10^{-2}n(r)$.

A simple analysis of the echo based on passive tracer particles orbiting at rate $\omega_E(r)$ quantitatively predicts all of the basic echo characteristics. The applied excitation voltages V_i, V_s are modeled as impulsively applied at $t = 0$ and $t = \tau$:

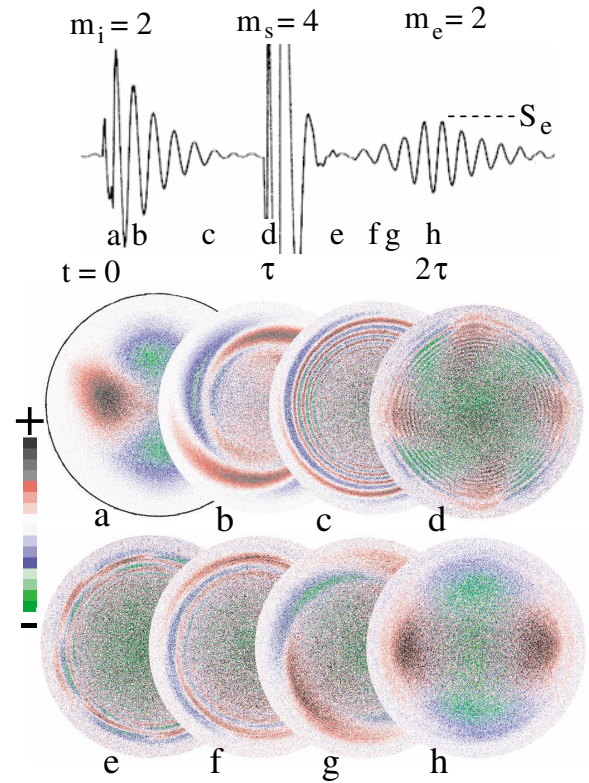


FIG. 2 (color). The top image shows the measured wall signal; below are experimental density perturbation images at eight successive times, corresponding to the times marked in the top trace.

$$\delta\phi_{\text{ext}}(r, \theta, t) = a_i V_i \Delta t_i \delta(t) \left(\frac{r}{R_w}\right)^{m_i} e^{-im_i\theta} + a_s V_s \Delta t_s \delta(t - \tau) \left(\frac{r}{R_w}\right)^{m_s} e^{im_s\theta}, \quad (3)$$

where $(a_i, a_s) = (0.55, 0.49)$ relate the voltages (V_i, V_s) applied on discrete wall sectors to the (m_i, m_s) spatial Fourier components. Here, the $+$ sign is chosen on $im_s\theta$ as that which yields the echo. Effectively, the θ -electric field from these applied potentials causes an instantaneous θ -dependent radial displacement of all plasma particles.

For $0 < t < \tau$, the first-order density perturbation $\delta n_i^{(1)}$ resulting from the initial wall excitation is obtained from Eqs. (2) and (3) and is

$$\delta n_i^{(1)}(r, \theta, t) = a_i V_i \Delta t_i \left(\frac{r}{R_w}\right)^{m_i} im_i \frac{c}{rB} \frac{\partial n_0}{\partial r} \times \exp[-im_i\theta + im_i\omega_E(r)t]. \quad (4)$$

At large t the term $e^{im_i\omega_E(r)t}$ becomes a rapidly oscillating function of r , so it generates minimal potential at the wall. This phase-mixing process is explicitly seen in Figs. 2(a)–2(c). The second wave excited at $t = \tau$ similarly damps due to phase mixing.

The basic echo response is seen in second order, as

$$\delta n_e^{(2)} \propto V_i V_s \tau \exp\left[im_e\theta - im_e\omega_E(r)\left(t - \tau \frac{m_s}{m_e}\right)\right], \quad (5)$$

where $m_e \equiv m_s - m_i$. This is extended to higher orders in Eq. (7).

Equation (5) predicts the mode number of the echo, giving $m_e = 2$ in Fig. 2. Experiments with a variety of (m_i, m_s) show $m_e = m_s - m_i$, and no echo is seen if $m_i > m_s$. Equation (5) also predicts the appearance time of the echo. The echo occurs when a macroscopic radial electric field exists at the wall, i.e., when the radial integral of the second-order perturbation does not phase mix to zero. Setting the r -dependent terms in the exponent in Eq. (5)

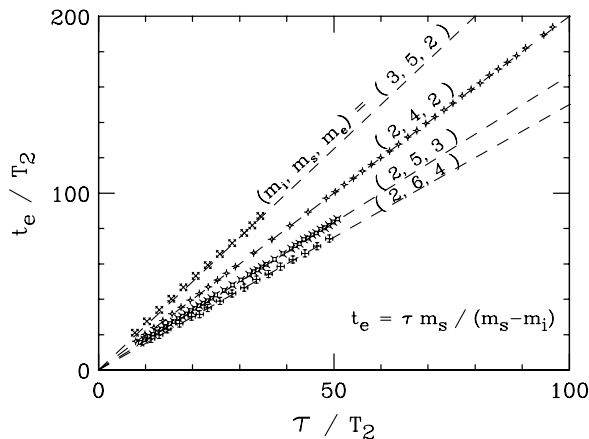


FIG. 3. Echo appearance time t_e versus the second wave launch time τ , both normalized to the $m = 2$ wave period T_2 , using various mode numbers.

to zero yields the time of the echo

$$t_e = \tau \frac{m_s}{m_s - m_i}. \quad (6)$$

We measure the echo appearance time t_e with an automated fit to the wall signal, using a symmetric growing and damping sine wave centered at t_e . Figure 3 shows the measured time of the echo response t_e versus the time of the second wave excitation τ , both normalized to the $m = 2$ wave period T_2 . The dashed lines are Eq. (6).

The peak amplitude S_e of the received echo depends on τ , as shown in Fig. 4. For small τ (here, for $\tau \lesssim 40T_2$), we find that $S_e \propto V_i V_s \tau$ as predicted by Eq. (5); and the proportionality with V_i and V_s has been verified separately over ranges of $10\times$ in each amplitude.

For larger excitation amplitudes, we calculate the ballistic trajectories including effects associated with non-linear bunching [5], giving a peak echo wall signal

$$S_e^{nc} = \int_0^{R_w} dr \alpha(r) V_i J_1[\beta(r) V_s \tau], \quad (7)$$

where α and β are given by

$$\alpha(r) \equiv G a_i \Delta t_i \epsilon \frac{ecm_i m_e}{2BR_w} \left(\frac{r}{R_w}\right)^{m_i + m_e} n_0(r) \frac{\partial \omega_E}{\partial r}, \quad (8)$$

$$\beta(r) \equiv a_s \Delta t_s m_i m_s \frac{c}{Br} \left(\frac{r}{R_w}\right)^{m_s} \frac{\partial \omega_E}{\partial r}.$$

The gain is given by $G \equiv (A/C)\tilde{G}$, where A is the area and C is the capacitance of the detection sectors, and where \tilde{G} is the amplifier gain. The small quantity ϵ represents the difference between t_e and the measurement time, which is defined as the time of the maximal echo wall signal (typically within one or two plasma rotation periods of t_e).

The echo amplitude is predicted to exhibit recurring ‘‘saturation’’ effects, shown dashed in Fig. 4. The early-time saturation effect is observed experimentally over a wide range of parameters, but the recurring saturation

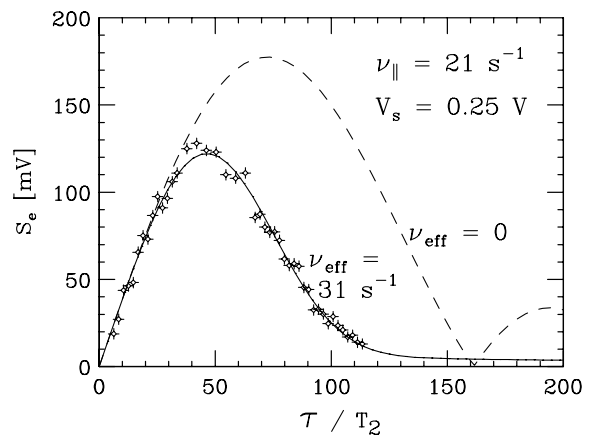


FIG. 4. Measured peak echo wall signal S_e versus the second wave launch time τ . The solid line shows the collisional theory of Eq. (9); the dashed line has $\nu_{\text{eff}} = 0$.

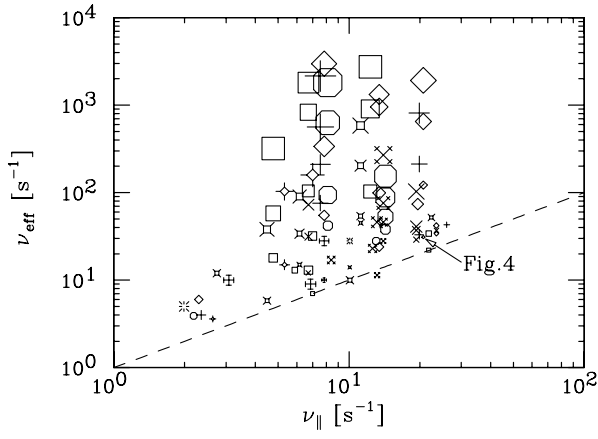


FIG. 5. Effective collision rate ν_{eff} obtained from fitting echo measurements to Eq. (9) versus the actual rate ν_{\parallel} .

effect (second bump) is typically not observed, either due to collisions (as in Fig. 4) or large amplitude effects.

To analyze collisional velocity scatterings and $\omega_E(r, v_z)$ effects, the nonlinear ballistic theory is combined with a second-order collisional theory. This predicts that near the echo appearance time t_e , the peak echo wall signal is

$$S_e^{\text{col}} = \int_0^{R_w} dr \alpha(r) V_i \frac{r}{n_0} \frac{\partial n_0}{\partial r} J_1[\beta(r) V_s \tau] \frac{1}{2\sqrt{\pi T}} \int_0^\infty \frac{d\varepsilon_z}{\sqrt{\varepsilon_z}} \times \exp[-\varepsilon_z/T - \gamma^3 \tau^3], \quad (9)$$

where the collisional damping is given by

$$\gamma^3(\nu_{\text{eff}}, r, \varepsilon_z) \equiv \nu_{\text{eff}} \frac{n(r)}{n(0)} \left(\frac{cT}{eBr} \right)^2 \left(\frac{1}{L} \frac{\partial L}{\partial r} \right)^2 \frac{8}{3} \frac{m_i^2 m_s}{m_e}, \quad (10)$$

the axial energy (at $z = 0$) is $\varepsilon_z \equiv M v_z^2/2$, and $L(r, \varepsilon_z)$ is the electron's z -bounce length, defined by

$$e\phi(r, \pm L/2) - e\phi(r, 0) = \varepsilon_z. \quad (11)$$

This collisional damping depends on the plasma end curvature, described by $\partial L/\partial r$.

We obtain an “effective” collision rate ν_{eff} by fitting S_e^{col} from Eq. (9) to data sets of measured $S_e(\tau)$, with ν_{eff} and the coefficients of α and β as fitting parameters. The solid line of Fig. 4 is Eq. (9) with $\nu_{\text{eff}} = 31 \text{ s}^{-1}$. This is close to the electron-electron scattering rate [14] of $\nu_{\parallel} = 21 \text{ s}^{-1}$, where

$$\nu_{\parallel} \equiv 2.8\sqrt{\pi n} \bar{v} b^2 \ln(r_L/b), \quad (12)$$

with $r_L \equiv \bar{v}/\Omega_c$ and $b \equiv e^2/T$.

Figure 5 plots this effective collisionality ν_{eff} for all our echo measurements versus the actual collisionality ν_{\parallel} at the (known) plasma density and temperature. Here, the density is varied over a factor of 10, and the temperature is varied by a factor of 2. In Fig. 5, the 50 \times range of the second wall excitation V_s is (logarithmically) represented by the size of the data symbol. At a given value of ν_{\parallel} ,

identical symbols of different sizes correspond to identical plasma parameters, but with different V_s .

Figure 5 shows that the echo lifetime is limited by collisional irreversibility of end-field θ smearing when the second wave excitation is sufficiently small. At large second wave amplitudes, a different (unknown) effect destroys the echo as effectively as collisions enhanced by 100 \times . Note that a 100 \times increase in ν_{eff} represents a mere 4.6 \times reduction in the echo viability time, because of the $\gamma^3 \tau^3$ scaling in Eq. (9).

In summary, we have observed fluid echoes in a pure electron plasma, explicitly demonstrating the reversible nature of spatial Landau damping. The phase mixing and unmixing associated with wave damping and echo generation are imaged directly, and the echo mode number, appearance time, and saturation effect agree with a simple ballistic theory. The pure electron plasma behaves like an ideal 2D fluid, despite 3D end effects that make ω_E dependent on an electron's z velocity. Different velocity classes separately phase mix and unmix, surprisingly forming the same echo. At late times the echo is degraded, and collisional scattering between velocity classes gives a fundamental limit to the echo lifetime.

This work was supported by NSF/DOE Grant No. PHY-0354979.

-
- [1] E. L. Hahn, Phys. Rev. **80**, 580 (1950).
 - [2] R. W. Gould, Am. J. Phys. **37**, 585 (1969).
 - [3] I. D. Abella, N. A. Kurnit, and S. R. Hartman, Phys. Rev. **141**, 391 (1966).
 - [4] J. H. Malmberg, C. B. Wharton, R. W. Gould, and T. M. O'Neil, Phys. Fluids **11**, 1147 (1968); A. Y. Wong and D. R. Baker, Phys. Rev. **188**, 326 (1969).
 - [5] T. M. O'Neil and R. W. Gould, Phys. Fluids **11**, 134 (1968).
 - [6] L. K. Spentzouris, J. F. Ostiguy, and P. L. Colestock, Phys. Rev. Lett. **76**, 620 (1996).
 - [7] O. Bruning, T. Linnecon, F. Ruggio, W. Scandale, and E. Shaposhnikov, *Nonlinear and Collective Phenomena in Beam Physics* (AIP, New York, 1997), p. 155.
 - [8] C. F. Driscoll and K. S. Fine, Phys. Fluids B **2**, 1359 (1990).
 - [9] H. Lamb, *Hydrodynamics* (Dover, New York, 1932), 6th ed., Secs. 158 and 159; W. Thomson (Lord Kelvin), Philos. Mag. **10**, 155 (1880).
 - [10] R. W. Gould, Phys. Plasmas **2**, 2151 (1995); D. A. Bachman, Ph.D. dissertation, California Institute of Technology, 1997.
 - [11] R. H. Levy, Phys. Fluids **8**, 1288 (1965); R. J. Briggs, J. D. Daugherty, and R. H. Levy, Phys. Fluids **13**, 421 (1970).
 - [12] D. A. Schecter *et al.*, Phys. Fluids **12**, 2397 (2000).
 - [13] A. J. Peurrung and J. Fajans, Phys. Fluids B **5**, 4295 (1993).
 - [14] S. Ichimaru, *Basic Principles of Plasma Physics* (W. A. Benjamin, Inc., Reading, 1973), p. 244.